A Robust Resonant Controller for High-speed Scanning of Nanopositioners: Design and Implementation

Jie Ling, Micky Rakotondrabe, *Member, IEEE*, Zhao Feng, Min Ming, and Xiaohui Xiao, *Member, IEEE*

***Abstract*—This paper presents a novel damping control scheme for piezo-actuated nanopositioning platforms with robust resonant control (RRC). The RRC is developed to attenuate the resonant-vibrational modes of the lightly damped dynamics of the stage in an inner positive feedback loop. The parameters in the proposed RRC are determined through an analytical approach. Indeed, the controller gains constrained by both the robustness and the damping ratio of the inner loop are tuned based on the small gain theory. Then, a high gain integral tracking controller is applied in the outer loop to minimize the tracking errors due to unmodeled nonlinearity and uncertainties. To validate the effectiveness of the proposed RRC, comparative experiments with conventional positive position feedback (PPF) and integral resonant control (IRC) are conducted on a piezo-actuated nanopositioning stage. Results demonstrate that the proposed RRC improves the closed-loop bandwidth from 67 Hz with PPF and 135 Hz with IRC to 176 Hz. Moreover, better robustness against load variations with a range of 0∼1000 g loading under 0∼20 Hz input raster scanning signals are obtained by RRC compared with PPF as well as IRC.**

***Index Terms*—Piezoelectric nanopositioner, resonant control, high-speed scanning, robustness.**

I. Introduction

Nanopositioners have been widely used in high-precision positioning applications, including, but not limited to, microrobotics, microassembly, microlithography, micromanipulation, microfabrication, microscopy scanning [1]–[3]. Owing to the merits of fast dynamics, large output forces and sub-nanometer resolution, piezoelectric ceramics are commonly applied to actuate these nanopositioners [4]. Unfortunately, the operating bandwidth of a piezo-actuated nanopositioner is usually limited to 10-100 times lower than the lowest resonant frequency because of its lightly damped resonant-vibrational modes [5], [6].

Different control approaches have been raised for damping the resonant modes and high-bandwidth tracking of piezo-actuated nanopositioners [7]. Among them, feedback architectures are most widely used for the superiority on robustness against external disturbances and model uncertainties [8]. Some general strategies are reported in the literature to minimize the tracking errors during the processes of high-speed tasks, such as H_∞ control [9], adaptive control [10], linear quadratic Gaussian (LQG) control [11], etc. These approaches permitted to find the controllers that ensured robust performance when the Q-factor of the system was low. Conversely, once the Q-factor becomes large and the system presents a very light damping ratio, the finding of a controller that ensures high damping performance becomes difficult with these approaches [9]. Hence, other specific model-based strategies for piezo-nanopositioners were developed with prioritized focus on damping control. These include: recursive delayed position feedback (RDPF) [5], robust mass damper (RMD) [12], model reference control (MRC) [13].

In addition to the above works, negative-imaginary control is a class of control approaches that are applicable to deal with problems of resonant vibrations of flexible structures with lightly damped modes [14], [15]. The negative imaginary theory provides a solution to increase damping of the vibrational modes as well as to maintain the robustness against modal uncertainty and unmodeled dynamics simultaneously [15]. A number of well-performing damping controllers based on negative-imaginary theory have then been developed to damp resonant modes but also to increase the bandwidth of the piezo-nanopostioners. These efforts include: passive shunt-damping (PSD) [13], positive position feedback (PPF) [16], positive velocity and position feedback (PVPF) [17], resonant control (RC) [18], integral resonant control (IRC) [19], [20] and so on. All the imaginary controllers mentioned above have fixed structures with low order and low computational complexity, which makes them simple in design and implementation. Moreover, when implementing the control laws using digital signal processing equipments, the property of fixed structure and low order allows for the highest possible sampling frequency [13]. However, apart from the IRC and the IFF approaches, a primary drawback of the other controllers lies in that these controllers are designed to damp each resonant mode separately. For a system with only one dominant mode (generally the first resonant mode), these controllers can be applicable with low order. But, for a system with multimode resonant frequencies, these controllers will lead to high order, which is not practical to implement [20]. Different from IFF, which needs additional sensors, IRC is more flexible. Therefore, among the aforementioned approaches, IRC is the

This work was supported by Shenzhen Science and Technology Program under Grant JCYJ20170306171514468, National Natural Science Foundation of China under Grant 51375349, and China Postdoctoral Science Foundation under Grant 2018M642905.

Jie Ling, Zhao Feng, Min Ming and Xiaohui Xiao are with the Hubei Key Laboratory of Waterjet Theory and New Technology, Wuhan University, Wuhan 430072, China. Xiaohui Xiao is also with Shenzhen Institute of Wuhan University, Shenzhen 518057, China. (e-mail: respectively, {jamesling, fengzhaozhao7, mingmin_whu, xhxiao}@whu.edu.cn).

Micky Rakotondrabe is with the FEMTO-ST Institute, Universit Bourgogne Franche-Comt/ENSMM/CNRS, Besanon 25000, France (e-mail: mrakoton@femto-st.fr).

most applicable damping approach for both systems with unique vibrational mode and with multi resonant modes.

In general IRC design, a feed-though term is added to induce a new pair of resonant zeros at a frequency below the first resonant mode. A simple integrator is then applied in the positive feedback loop to damp the vibrational modes. With the increasing of the controller gain, poles of the closed-loop will move away from the imaginary until the damping ratio reaches a peak point [19], [20]. As these two parameters (feedthrough term and controller gain) in the IRC scheme can be calculated and determined analytically if the transfer function of the nominal system is identified as demonstrated in [20], it is simple and practical for users to design and implement the controller. However, for piezo-actuated nanopositioners applied on those occasions, where the variation of loaded mass or environmental temperature leads to significant changes in nominal resonant frequency, the standard IRC designed on the basis of nominal system may result in unsatisfied performance against uncertainty. Inspired by the efforts for standard IRC in [19], [20], a novel robust resonant controller consisting of a feed-through term and a second order damping controller is proposed in this paper.

The contributions of this brief are threefold. First, a second order damping controller is integrated with a feed-through term to synthesis a novel robust resonant controller (RRC). It should be noted that the second order damping controller in the proposed RRC is referred from PPF [16] for its high robustness against uncertainty. For this, the proposed RRC structure as well as its objective is totally different from the existing band-pass filter in IRC scheme, which is also a second order damper. Second, the analytical relationship between controller parameters is derived. Then, a tradeoff between closed-loop bandwidth and damping ratio based on small gain theory is proposed for controller design. Third, an illustrative example with a piezo-actuated nanopositioner accompanied by experiments and discussions is presented. The robustness of the proposed RRC is studied by simulations and experiments. Comparison with existing PPF and IRC schemes under different load variations on the platform are also conducted.

The rest of this brief is organized as follows. The existing standard IRC scheme is reviewed in Section II. Then, Section III describes the design of the proposed RRC. The experimental setup and the system identification are presented in Section IV. Verifications and discussions are shown in Section V. Finally, Section VI concludes this paper.

II. Conventional IRC Scheme

Assuming a piezo-actuated nanopositioner with a lightly damped mode, the dominant dynamics can be approximately identified as a second-order system as,

$$G(s) = \frac{\sigma^2}{s^2 + 2\xi_n\omega_n \cdot s + \omega_n^2} \tag{1}$$

where, s is the Laplace operator for continuous system, σ^2 is the gain of this resonant mode, ξ_n is the damping coefficient, and ω_n is the natural frequency. In this system, $\xi_n \ll 1$, which indicates that the resonant mode around the frequency of ω_n is lightly damped.

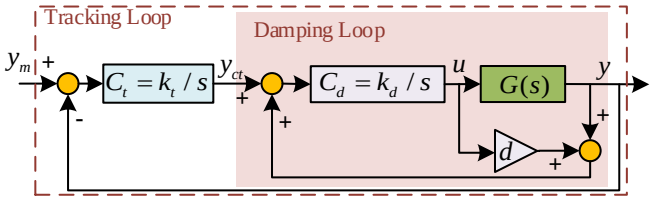

Fig. 1. Conventional IRC scheme.

Figure 1 shows the conventional IRC scheme, where G is the identified model, C_d is the damping controller, C_t is the tracking controller, d is a feedthrough term, y_m, y_{ct} and y are the input references, tracking controller output and closed-loop output, respectively. Here, the inner loop from y_m to y is denoted as the damping loop with a transfer function as,

$$T_{damp}(s) \triangleq \frac{C_d(s) \cdot G(s)}{1 - C_d(s) \cdot (G(s) + d)}. \tag{2}$$

The damping controller gain k_d is found to maximize the damping ratio of the damping loop, which can be calculated by

$$k_d|_{\xi_{max}} = \frac{1}{|d|}\left(\omega_n \cdot \sqrt{\frac{\omega_n}{\omega_n^2 + \sigma^2/d}}\right) \tag{3}$$

where, ξ_{max} is the achievable maximum damping ratio, the feedthrough term can be chosen as $d = -2\sigma^2/\omega_n^2$.

For the tracking controller design, the gain should obey the following inequality,

$$k_t \cdot k_d < -\frac{\sigma^2 + d \cdot \omega_n^2}{d^2}. \tag{4}$$

It is notable that only the inner damping loop in (2) is related to damp the resonant-vibrational mode of (1). The tracking controller in external loop is used to minimize tracking errors especially in the low frequency region.

For conventional IRC parameters' selection and tuning, the model uncertainty resulted from load variation or surrounding environmental change is considered neither in the original design approach [19] nor in the improved analytical design approach [20]. Therefore, the robustness against uncertainty of the conventional IRC needs to be improved, which will be experimentally verified in Section V.

III. Proposed Robust Resonant Control Scheme

In this section, a new control scheme named RRC is suggested. Besides, the design process for parameters in the RRC is discussed analytically.

As depicted in Fig. 2, inspired by PPF control and IRC control, we propose a robust second order controller in the inner damping loop to replace the simple integral damper in the conventional IRC. In the outer loop, a commonly used tracking controller is applied to eliminate tracking errors. Parameters in the damping controller will be discussed through an analytical approach, and the controller gains will be tuned based on the small gain theory in following subsections.

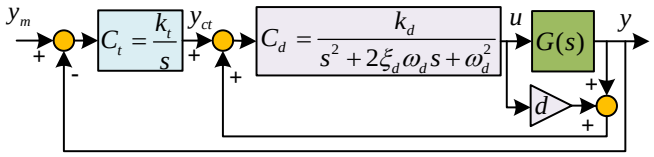

Fig. 2. Proposed RRC scheme.

A. Parameter Selection

1) Feedthrough term d: The purpose of adding a feedthrough term is to induce a pair of zeros in the root locus of the damping loop in (2). With the increasing of controller gain, the root locus will start from the natural poles and end at the added resonant zeros, where a maximum damping ratio can always be found for the resonant mode. Furthermore, for a collocated system with multi resonant modes, e.g. a piezoelectric cantilever beam, the adding of a feedthrough term results in compound dynamics with interlaced zeros then poles. Then, all the resonant modes can be damped consistently when tuning controller gain. This is well explained and analyzed in [20]. In the RRC scheme, the feedthrough term is chosen as the same with IRC as $d = -2\sigma^2/\omega_n^2$.

2) ω_d and ξ_d: Considering the damping loop in (2) by replacing the damping controller with a second order damper in Fig. 2, there are four poles with two from the natural system and the other two resulted from the damping controller, and two zeros induced from the added feedthrough term. For this, the root locus of the damping loop will have four trajectories, among which four trajectories start from the four poles while two trajectories end at the induced zeros and two trajectories end at infinity. Figure 3 displays the three possible cases of the root locus of the damping loop with different values of the two parameters (i.e., ω_d and ξ_d). The three states are named *'Ordered', 'Critical' and 'Chaotic'*, respectively. To damp the multi resonant modes of a collocated system simultaneously and consistently, the root locus of the damping loop need to follow the ordered trajectories as shown in Fig. 3(a), which means that all the resonant modes start from the natural poles and end at the induced zeros, while the two roots induced by the damping controller move to infinite points.

For this, the proper range for ω_d and ξ_d need to be found so that the resulted root locus of the damping loop would follow the ordered trajectories. Considering the critical state in Fig. 3(b), there is a pair of complex breakaway points in this state, which means that the characteristic equation of the damping loop has a pair of complex identical roots. Herein, we can obtain a relationship between ω_d and ξ_d through solving the characteristic equation of the damping loop $1 - G_d \cdot (G + d) = 0$. Applying the RRC controller in Fig. 2 into this equation, we have

$$1 - \frac{d\left(s^2 + 2\xi_n\omega_n s + \omega_z^2\right)}{s^2 + 2\xi_n\omega_n s + \omega_n^2} \cdot \frac{k_d}{s^2 + 2\xi_d\omega_d s + \omega_d^2} = 0. \quad (5)$$

where, $\omega_z^2 = \sigma^2/d + \omega_n^2$ represents the induced zeros by the feedthrough term. Rearranging (5), the characteristic equation will be of the following form as,

$$P(s) = s^4 + K_3 \cdot s^3 + K_2 \cdot s^2 + K_1 \cdot s + K_0 \quad (6)$$

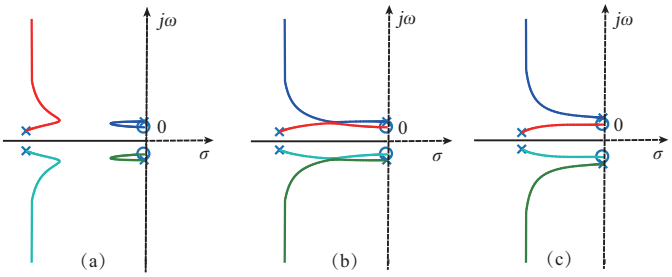

Fig. 3. Root locus of the damping loop with RRC. (a) The trajectory of resonant mode starts from the natural poles and ends at induced zeros by the feed-through term (*Ordered state*). (b) The trajectories have a pair of complex breakaway points (*Critical state*). (c) The trajectories start from the natural poles and do not end on induced zeros (*Chaotic state*).

with

$$\begin{cases} K_3 = 2\xi_d\omega_d + 2\xi_n\omega_n \\ K_2 = \omega_d^2 + 2\xi_d\omega_d \cdot 2\xi_n\omega_n + \omega_n^2 - d \cdot k_d \\ K_1 = \omega_d^2 \cdot 2\xi_n\omega_n + 2\xi_d\omega_d \cdot \omega_n^2 - d \cdot k_d \cdot 2\xi_n\omega_n \\ K_0 = \omega_d^2 \cdot \omega_n^2 - d \cdot k_d \cdot \omega_z^2. \end{cases}$$

For the damped system with a pair of complex identical roots in the left half plane as Fig. 3(b) describes, its characteristic equation should have the following form as,

$$\begin{aligned} P^*(s) &= (s^2 + \alpha \cdot s + \beta)^2 \\ &= s^4 + 2\alpha \cdot s^3 + (\alpha^2 + 2\beta)s^2 + 2\alpha\beta \cdot + \beta^2, \end{aligned} \quad (7)$$

where, $\alpha < 0$ and $\Delta = \alpha^2 - 4\beta < 0$ for a repeated pair of complex roots.

Let $P(s) = P^*(s)$, and solve the equation set, an analytical relationship between the parameters in damping controller can be obtained as,

$$\begin{aligned} &F_1(k_d, \xi_d, \omega_d) = \omega_d^2 + 2\xi_d\omega_d \cdot 2\xi_n\omega_n + \omega_n^2 - (\xi_d\omega_d + \xi_n\omega_n)^2 \\ &- \left(\omega_d^2 \cdot 2\xi_n\omega_n + \omega_n^2 \cdot 2\xi_d\omega_d - d \cdot k_d \cdot 2\xi_n\omega_n\right) / (\xi_d\omega_d + \xi_n\omega_n) \\ &- d \cdot k_d = 0, \end{aligned} \quad (8)$$

and

$$\begin{aligned} &F_2(k_d, \xi_d, \omega_d) = \omega_d^2 \cdot \omega_n^2 - d \cdot k_d \cdot \omega_z^2 \\ &- \left(\omega_d^2 \cdot 2\xi_n\omega_n + \omega_n^2 \cdot 2\xi_d\omega_d - d \cdot k_d \cdot 2\xi_n\omega_n\right)^2 / (\xi_d\omega_d + \xi_n\omega_n)^2 \\ &= 0. \end{aligned} \quad (9)$$

Two implicit functions F_1 and F_2 with respect to k_d, ω_d and ξ_d can be obtained when solving for breakaway points occurred in the critical state in Fig. 3(b). By solving (8) and (9) for a further step, we can obtain the analytical relationship between ω_d and ξ_d, which will lead the system to critical state as shown in Fig. 3(b). The relationship can be plotted as Fig. 8 in Section V, where the solid boundary stands for the values of ω_d and ξ_d to lead the system to critical state.

Remark 1: To determine a specific set of the two parameters of ω_d and ξ_d, a tradeoff between the bandwidth and the achievable maximum damping ratio of the damping loop should be made. For this, a discussion is presented in the case studies in Section V.

B. Damping Controller Gain Tuning

In conventional IRC design, the controller gain is tuned to achieve the maximum damping ratio as stated before.

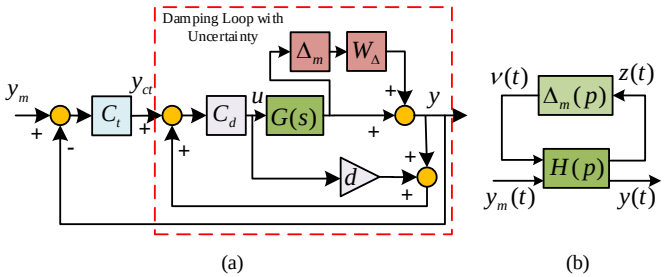

Fig. 4. RRC with multiplicative uncertainty. (a) Closed-loop scheme. (b) Augmented system.

However, the system uncertainty is not taken into consideration in the design process. In the proposed RRC design, we propose to determine the damping controller gain considering two conditions, i.e., a) damping condition as described in (3), b) robustness condition based on small gain theory.

Theorem 1: The closed loop system under RRC control with multiplicative uncertainty shown in Fig. 4(a) is internally stable for all uncertainty $\|\Delta_m(s)\| \leq 1$ if and only if

$$\left\| \frac{C_d \cdot G}{1 - C_d \cdot (G + d)} \cdot W_\Delta \right\| < 1, \tag{10}$$

where W_Δ is the weighting function of the uncertainty, which is designed to surpass the measured uncertainty as

$$\|\Delta_m(s) \cdot W_\Delta\| > \|\Delta(s)\|, \tag{11}$$

for all frequencies. $\Delta(s)$ is the multiplicative uncertainty which can be obtained by measuring the perturbed system under different loaded masses and calculated by (13).

Remark 2: By performing an upper linear fractional transformation and converting the system in Fig. 4(a) into an augmented format as shown in Fig. 4(b), then, Theorem 1 can be derived based on the small gain theory as described in [21, Ch. 9].

Hereto, the damping controller gain in the proposed RRC can be determined based on the damping condition as well as the robustness condition in (10).

C. Tracking Controller Gain Tuning

As displayed in Fig. 2, the inner damping loop can only alleviate the resonant vibrations caused by the lightly damped modes. A tracking controller in the outer loop needs to be utilized to deal with the hysteresis and the creep nonlinearity to decrease the tracking errors. Considering the ease of calculation and implementation, a high-gain feedback integral is adopted in the outer loop of the proposed RRC, which is also a widely used approach in [5], [13], [17], [19], [20].

With respect to the tracking controller gain tuning, a graphical method is introduced in [5], for the determination of the PI control gains. In the RRC design, the maximum allowable overshoot and the settling time of the step response of the closed-loop system are given first. The tracking controller gain is tuned by trial and error method as well as the graphical method to check that the simulated responses agree with the desired performance.

D. Overall Procedure

The overall procedure for the RRC design can be summarized in the following steps:

- *Step 1:* Perform a set of system identifications with a set of load variations (including no loading as the nominal system) and obtain a transfer function model for the nominal system as expressed in (1) as well as a set of systems with perturbation.
- *Step 2:* Calculate the feed though term d according to (3) to add a pair of resonant zeros followed by the natural poles of the controlled plant as shown in Fig. 3.
- *Step 3:* Plot the state figure for the damping loop based on (8) and (9) to find the proper range for ω_d and ξ_d to lead the system to an ordered state as displayed in Fig. 3(a). The state figure may refer to Fig. 7 in Section V. Determine a candidate range of ω_d and ξ_d based on achieved bandwidth of the damping loop.
- *Step 4:* Plot the figure of achievable maximum damping ratio versus ω_d and ξ_d (See Fig. 8). Make a tradeoff between achievable bandwidth and maximum damping ratio and determine a set of ω_d and ξ_d.
- *Step 5:* Calculate the multiplicative uncertainty G_Δ and design the weighting function W_Δ. Tune the damping controller gain k_d to satisfy the damping condition and the robustness condition in (10). (See Fig. 9).
- *Step 6:* Tune the tracking controller gain k_t based on trial and error method to achieve desired step response performances.

IV. Experimental Setup and System Identification

A. Experimental Setup

The designed controller is implemented on a three-axis piezo-actuated nanopositioning stage (model P-561.3CD from Physik Instrumente) as shown in Fig. 5. The terminal motion produced by the actuator is within 0–100 μm for each individual axis. The control input voltage (0–10 V) for each axis is produced by 16-bit digital to analog interfaces (DACs) of the data output module in dSPACE MicroLabBox and subsequently amplified via a piezo amplifier module (model E-503.00 from Physik Instrumente) with a fixed gain of 10 to provide excitation voltage (0–100 V). The displacement of the output is measured via a PZT servo submodule (model E-509.C3A from Physik Instrumente) and is passed to the data input module in dSPACE MicroLabBox with 16-bit analog to digital interfaces (ADCs). Details about the signal flow are given in Fig. 5(b). The control algorithm is designed in Matlab/Simulink block diagram on the host PC, and then downloaded and executed on the target dSPACE MicroLabBox in the real-time software environment of dSPACE ControlDesk.

In this work, only the y-axis was used to implement the proposed controller and the sampling frequency of the system was set to 10 kHz.

B. System Identification

1) Nominal model: A linear model of the y-axis was obtained by applying a step voltage at 10 V into the electrode and

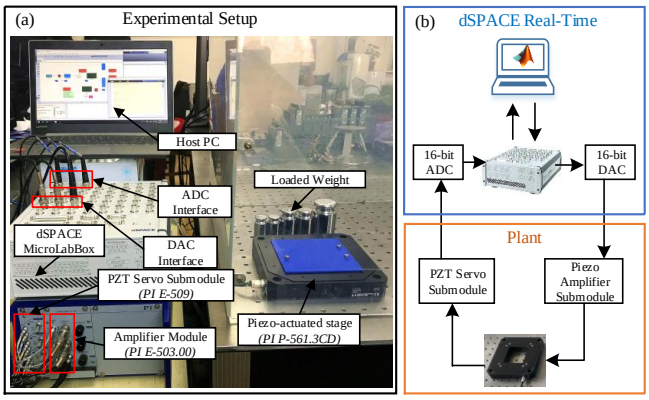

Fig. 5. The experimental setup of the piezo-actuated nanopositioning stage (a) Experimental platform (b) Block diagram of the signal flow.

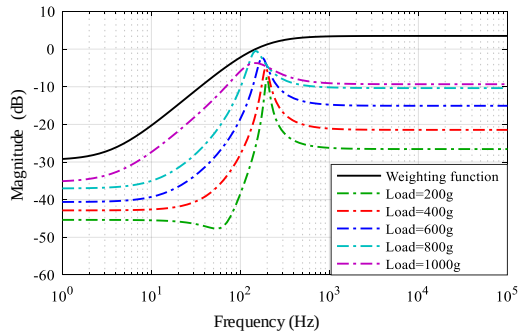

Fig. 6. Multiplicative system uncertainty with load variations and the designed weighting function

recording the corresponding sensor output. Then, the system identification toolbox in MATLAB was used to identify the dynamic model. The obtained continuous transfer function of the dominant dynamics is displayed in (12) with the frequency response described in Fig. 10(a). The first resonant mode of the system with no load occurs at the frequency of 205 Hz with a magnitude of 18.5 dB, where the damping controller is to be designed to reject the unexpected vibrations.

$$G(s) = \frac{y(s)}{u(s)} = \frac{1.198 \times 10^6}{s^2 + 110s + 1.673 \times 10^6}, \tag{12}$$

where $y[\mu m]$ is the output displacement and $u[V]$ is the driving voltage.

2) Perturbed model: A set of system identifications were conducted to obtain perturbed models under different loaded masses. Identified system models with load variations are displayed in Fig. 10(a). Corresponding multiplicative uncertainties shown in Fig. 6 are calculated by,

$$\Delta(s) = G_p(s)/G(s) - 1, \tag{13}$$

where $G(s)$ is the identified nominal model in (12), $G_p(s)$ is the perturbed model with load variations. The weighting function, which is also presented in Fig. 6, is designed as

$$W_\Delta(s) = \frac{s + 23.15}{0.6683s + 691.2}. \tag{14}$$

V. Evaluations and Discussions

In this section, the conventional IRC, PPF and the proposed RRC are designed on the basis of identified dynamics of the piezo-actuated nanopositioner. Extensive comparisons between these controllers are conducted through tracking experiments where 5Hz, 10Hz, 20Hz Triangular scanning signals are used as inputs. In addition, the robustness against load variations are verified under a set of loaded masses including 200 g, 400 g, 600 g, 800 g and 1000 g mass.

A. PPF, IRC and RRC Design

To make fair comparisons, the rise time and the overshoot of step responses of the closed-loop systems are set less than 8 ms and 3% for each control scheme. The damping controller in each scheme is chosen to achieve the maximum damping ratio for the resonant mode, while in RRC design, an additional robustness condition is considered. The tracking controller in each scheme is designed to obtain desired performance mentioned above.

1) PPF Controller: Utilizing the pole placement approach introduced in [16], designed poles are chosen through shifting -1000 units of poles in (12) along with real axis in the complex plane. The PPF controller is obtained as

$$C_d^{PPF} = \frac{4.187 \times 10^6}{s^2 + 6519s + 7.628 \times 10^6}, \quad C_t^{PPF} = \frac{250}{s}.$$

2) IRC Controller: According to (3) and (4), the conventional IRC is designed as

$$d = -1.43, \quad C_d^{IRC} = \frac{1098}{s}, \quad C_t^{IRC} = \frac{258}{s}.$$

3) RRC Controller: In the proposed RRC, the first step is to determine the proper range of ω_d and ξ_d such that the root locus of the damping loop can follow the trajectory like an ordered state in Fig. 3(a). As the first resonance of the plant occurs at 205 Hz, we can assign a range for ω_d between 40–220 Hz, and the corresponding values of ξ_d can be obtained by (8) and (9). As depicted in Fig. 8, the black solid line shows results obtained by (8) and (9), which will lead the damping loop to the critical state. Parameters in the upper area are the proper range for ω_d and ξ_d in RRC. To determine the specific set of parameters, the achievable maximum damping ratio versus parameters are plotted in Fig. 8. It is found that the maximum achievable ξ_{max} occurs when ω_d and ξ_d are chosen in the critical state line in Fig. 7, which is the same with the blue dotted line in Fig. 8. Therefore, we should choose ω_d and ξ_d in the upper right neighborhood of the critical state line in Fig. 7. A tradeoff between the closed-loop bandwidth and the damping ratio should be made according to the tendency of the critical state line. In this experiment, designed values are $\omega_d = 163$ Hz and $\xi_d = 0.9$, and the achievable maximum damping ratio is $\xi_{max} = 0.3451$, which is superior than the IRC case as shown in Table. I.

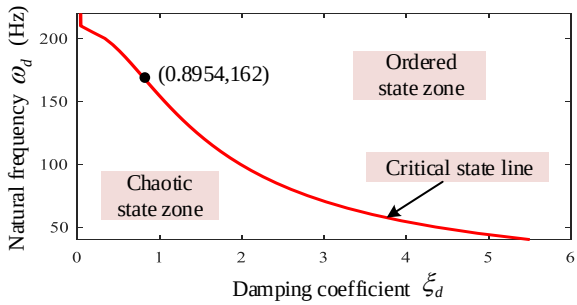

Fig. 7. The range of ω_d and ξ_d for three states in Fig. 3 of the piezo-actuated nanopositioner with RRC controller

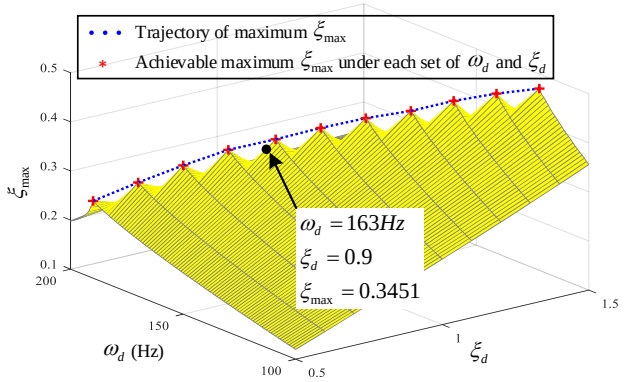

Fig. 8. The achievable maximum damping ratio for the resonant mode versus each set of ω_d and ξ_d

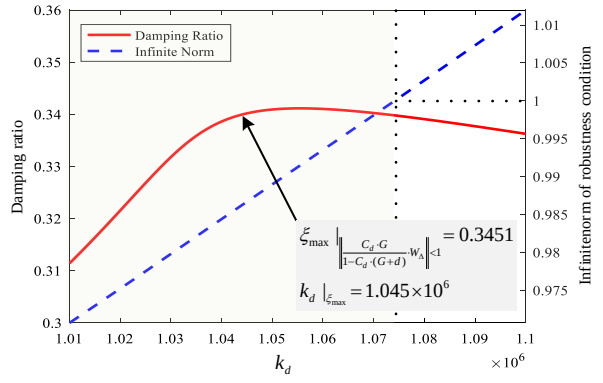

Fig. 9. Determination of damping controller gain k_d based on the damping condition and the robustness condition.

According to damping and robustness conditions, the damping controller gain can be determined as $k_d = 1.045 \times 10^6$ as shown in Fig. 9. Hereto, the designed RRC is

$$C_d^{RRC} = \frac{1.045 \times 10^6}{s^2 + 1840s + 1.044 \times 10^6}, \quad C_t^{RRC} = \frac{570}{s}.$$

B. Simulation Results

Before conducting experiments, comparisons of closed-loop bandwidth, damping ratio as well as robustness among three controllers (i.e., PPF, IRC and RRC) were performed through simulations based on identified nominal and perturbed models. Some performance indexes in both time and frequency domains of closed-loop systems with three controllers are shown in Table I. It can be found that all three controllers satisfy step response requirments set in Section V-A. Besides, all margin gains are larger than 2 dB and margin phases are larger than 30°, which implies that three designed controllers also meet basic margin conditions. Nevertheless, among these three controllers, the proposed RRC can obtain the maximum bandwidth of 176 Hz as well as the maximum damping ratio of 0.345 for the resonant mode.

TABLE I
FREQUENCY AND TIME DOMAIN INDEXES

Index	PPF	IRC	RRC
Bandwidth (Hz)	67	135	176
Margin gain (dB)	2.01	2.45	2.02
Margin phase (°)	78.27	68.64	73.40
Rise time ($m.s$)	6.71	3.37	2.86
Overshoot (%)	2.95	1.52	1.68
Damping ratio	0.221	0.268	0.345

In order to compare the robustness performance under load variations, system bode digrams and step responses are persented in Fig. 10. It can be clearly seen from Fig. 10(a) that the proposed RRC can guarantee more smooth frequency responses around the changed resonances due to load variations compared with IRC as well as PPF. Regarding step responses under different loads, it can be observed through Fig. 10(b) that the RRC can perform steadily and consistently with load uncertainties within 1000 g.

C. Experimental Results of Raster Tracking

To evaluate the tracking performance of three controllers, a set of raster scanning signals at 5, 10 and 20 Hz are fed into the platform. To evaluate and compare the performance directly using these three controllers, the feedback delay is identified and removed before quantitative analysis. For detailed descriptions about the processing of the delay, readers can refer to Eq. (2) in [23].

Tracking results of 0 g load under PPF, IRC and RRC are recorded in Fig. 11 and Table II. It can be seen that, for 0 g load, all three controllers can track raster signals well at 5 Hz and 10 Hz with the root mean square error (RMSE) value less than 0.015 μm, which acconts for less than 1% of the positioning stroke of 2 μm. For the 20 Hz case, the RMSE value with PPF and IRC are 0.051 μm and 0.038 μm, whereas the RMSE with RRC is 0.019 μm, which makes 63% and 50% improvements over PPF and IRC, respectively. The main reason for this is the achieved closed-loop bandwidth of RRC control is 176 HZ, which is the maximum one among the controller set as presented in Table I.

D. Experimental Results of Robustness Test

As displayed in Fig. 10(a), the worst situation with load variations is 1000 g, where the first resonance is shifted from 205 Hz to 139 Hz. Therefore, in this subsection, the 20 Hz triangular scanning signals is fed into the closed-loop system

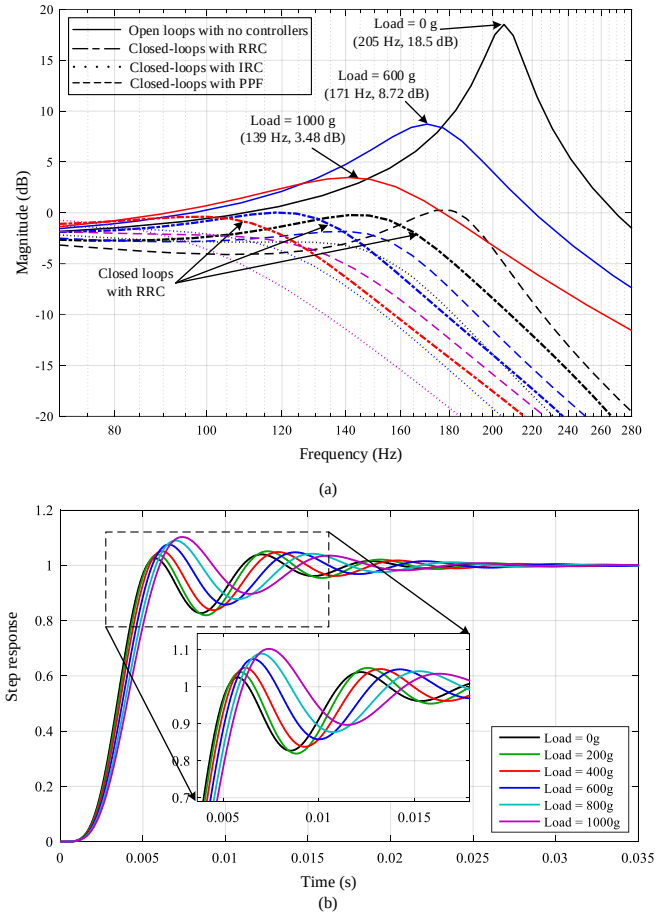

Fig. 10. Comparative results of open loops and closed-loops with PPF, IRC and RRC. (a)System bode diagrams at 0, 600 and 1000 g. (b)Simulation results of step responses with RRC from 0∼1000g

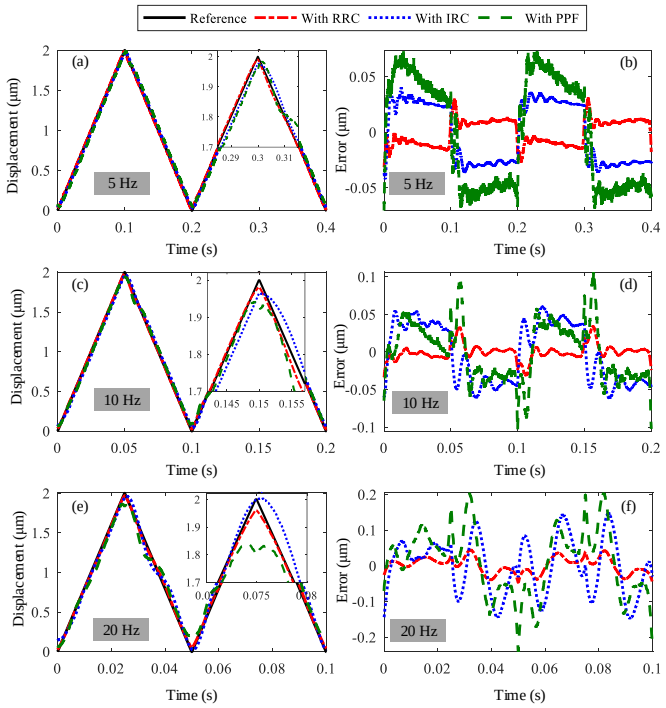

Fig. 11. Experimental results of outputs and tracking errors of raster references. (a)–(b) 5Hz. (c)–(d) 10Hz. (e)–(f) 20Hz.

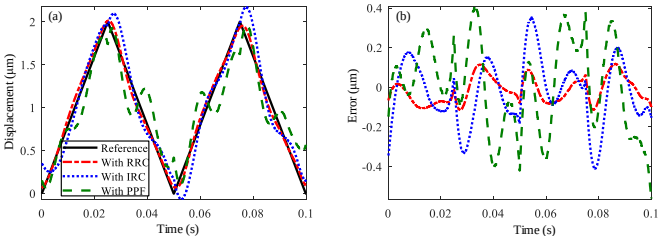

Fig. 12. Tracking results of 20 Hz triangular scanning signals for the system loaded with 1000 g mass.

under PPF, IRC and RRC control to test the robustness of three controllers. Simulated bode diagrams of the closed-loops systems are displayed in Fig. 10(a), and the time domain tracking results are depicted in Fig. 12. From Fig. 10(a), it can be found that the closed-loop system with RRC provides a flatter response compared with PPF and IRC, which is also proved by the tracking error results in Fig. 12. To be more specific, RMSEs of PPF and IRC are 0.128 and 0.099 μm, while the RMSE with RRC is only 0.033 μm (74% less than PPF and 67% less than IRC).

E. Discussions

More specific comparisons of tracking performance among PPF, IRC and RRC are recorded in Table II. Taking a closer look into the time domain RMSE, it can be seen that the proposed RRC performs better than PPF and IRC against load variations with a range of 0∼1000 g in the experiments. In the aforementioned experiments, triangular signals with a maximum frequency of 20 Hz are utilized, which is approximately ten times lower than the first resonance of the open loop dynamics. However, it is relatively a high working bandwidth for triangular signals, because they contain all odd harmonics of the basic frequency [7], [16–18], which are several times higher than 20 Hz in this case.

It should be noted that both IRC and RRC can deal with vibrational damping of collocated systems that contain multiple dominating resonant modes with only one controller, whereas each resonant mode needs to be damped by an

TABLE II
PERFORMANCE MEASURE

Reference frequency (Hz)	Load (g)	RMSE with PPF (μm)	RMSE with IRC (μm)	RMSE with RRC (μm)
5	0	0.014	0.009	0.005
5	600	0.012	0.010	0.015
5	1000	0.022	0.015	0.014
10	0	0.021	0.025	0.010
10	600	0.045	0.047	0.020
10	1000	0.065	0.051	0.030
20	0	0.051	0.038	0.019
20	600	0.084	0.080	0.023
20	1000	0.128	0.099	0.033

individual damping controller when utilizing PPF approach [19]. Moreover, the PPF scheme always need a nonlinear search for parameters' tuning, which is more complicated than the analytical approach used in IRC and RRC design. It is also worthy of noting that the proposed RRC scheme can provide better performance of robustness than conventional IRC, but the design process is a bit more complex as there are more parameters in the controller. Herein, for a system with already known load variations, such as applications in microassembling, cell manipulation, SPM scanning where consistent positioning performance under different loads are demanded, the proposed RRC can be considered as an alternative option for better robustness.

VI. Conclusion

This brief presents a new robust resonant control scheme for damping control of piezo-actuated nanopositioners. The RRC is applied in the inner damping loop to damp resonant-vibrational modes. In the outer loop, a high-gain integral tracking controller is utilized to decrease tracking errors. Parameters of the damping loop are determined through an analytical approach, and controller gains are tuned via a graphic method. The overall design procedure is given for designers. Finally, the developed RRC is applied to a piezo-actuated nanopositioner, to damp the resonant mode and to compare with the conventional PPF and IRC schemes by tracking raster scanning signals at different frequencies under load variations. Experimental results demonstrate the superiority of the proposed RRC controller.

References

[1] M. Rakotondrabe, and I. A. Ivan, "Development and dynamic modeling of a new hybrid thermopiezoelectric microactuator," *IEEE Trans. Robot.*, vol. 26, no. 6, pp. 1077–1085, Dec. 2010.

[2] O. T. Ghalehbeygi, A. G. Wills, B. S. Routley, and A. J. Fleming, "Gradient-based optimization for efficient exposure planning in maskless lithography," *J. Micro Nanolithogr. MEMS MOEMS*, vol. 16, no. 3, pp. 033507, Sept. 2017.

[3] P. Wang, and Q. Xu, "Design and testing of a flexure-based constant-force stage for biological cell micromanipulation," *IEEE Trans. Autom. Sci. Eng.*, vol. 15, no. 3, pp. 1114–1126, Jul. 2018.

[4] Q. Xu, "Precision motion control of piezoelectric nanopositioning stage with chattering-free adaptive sliding mode control," *IEEE Trans. Autom. Sci. Eng.*, vol. 14, no. 1, pp. 238–248, Jan. 2017.

[5] C. X. Li, Y. Ding, G. Y. Gu, and L. M. Zhu, "Damping control of piezo-actuated nanopositioning stages with recursive delayed position feedback," *IEEE ASME Trans. Mechatron.*, vol. 22, no. 2, pp. 855–864, Apr. 2017.

[6] J. Ling, Z. Feng, M. Ming, and X. H. Xiao, "Damping controller design for nanopositioners: a hybrid reference model matching and virtual reference feedback tuning approach," *Int. J. Precis. Eng. Man.*, vol. 19, no. 1, pp. 13–22, Jan. 2018.

[7] M. S. Rana, H. R. Pota, and I. R. Petersen, "A survey of methods used to control piezoelectric tube scanners in high–speed AFM imaging," *Asian J. Control*, vol. 20, no. 4, pp. 1379–1399, Jul. 2018.

[8] M. Rakotondrabe, "Multivariable classical PrandtlIshlinskii hysteresis modeling and compensation and sensorless control of a nonlinear 2-dof piezoactuator," *Nonlinear Dyn.*, vol. 89, no. 1, pp. 481–499, Jul. 2017.

[9] O. Aljanaideh, and M. Rakotondrabe, "Observer and robust H-inf control a 2-DOF piezoelectric actuator equipped with self-measurement," *IEEE Robotics and Automation Letters*, vol. 3, no. 2, pp. 1080–1087, Apr. 2018.

[10] J. A. Escareno, M. Rakotondrabe, and D. Habineza, "Backstepping-based robust-adaptive control of a nonlinear 2-DOF piezoactuator," *Control Eng. Pract.*, vol. 41, pp. 57–71, Aug. 2015.

[11] H. Habibullah, H. R. Pota, and I. R. Petersen, "A novel control approach for high-precision positioning of a piezoelectric tube scanner," *IEEE Trans. Autom. Sci. Eng.*, vol. 14, no. 1, pp. 325–336, Jan. 2017.

[12] K. Verbaan, van der Meulen, and M. Steinbuch, "Broadband damping of high-precision motion stages," *Mechatronics*, vol. 41, pp. 1–16, Feb. 2017.

[13] A. A. Eielsen, M. Vagia, J. T. Gravdahl, and K. Y. Pettersen, "Damping and tracking control schemes for nanopositioning," *IEEE ASME Trans. Mechatron.*, vol. 19, no. 2, pp. 432–444, Apr. 2014.

[14] I. R. Petersen, and A. Lanzon, "Feedback control of negative-imaginary systems," *IEEE Control Syst.*, vol. 30, no. 5, pp. 54–72, Oct. 2010.

[15] I. R. Petersen, "Negative imaginary systems theory and applications," *Annual Reviews in Control*, vol. 42, pp. 309–318, Sept. 2016.

[16] S. S. Aphale, B. Bhikkaji, and S. R. Moheimani, "Minimizing scanning errors in piezoelectric stack-actuated nanopositioning platforms," *IEEE Trans. Nanotechnol.*, vol. 7, no. 1, pp. 79–90, Jan. 2008.

[17] D. Russell, A. J. Fleming, and S. S. Aphale, "Simultaneous optimization of damping and tracking controller parameters via selective pole placement for enhanced positioning bandwidth of nanopositioners," *ASME J. Dyn. Syst. Meas. Control*, vol. 137, no. 10, pp. 101004, Jul. 2015.

[18] S. K. Das, H. R. Pota, and I. R. Petersen, "Resonant controller design for a piezoelectric tube scanner: A mixed negative-imaginary and small-gain approach," *IEEE Trans. Control Syst. Technol.*, vol. 22, no. 5, pp. 1899–1906, Sept. 2014.

[19] S. S. Aphale, A. J. Fleming, and S. R. Moheimani, "Integral resonant control of collocated smart structures," *Smart. Mater. Struct.*, vol. 16, no. 2, pp. 439–446, Feb. 2007.

[20] M. Namavar, A. J. Fleming, M. Aleyaasin, K. Nakkeeran, and S. S. Aphale, "An analytical approach to integral resonant control of second-order systems," *IEEE ASME Trans. Mechatron.*, vol. 19, no. 2, pp. 651–659, Apr. 2014.

[21] K. M. Zhou, J. C. Doyle, and K. Glove, "Modeling uncertainty and robustness," *Robust and optimal control.* Englewood Cliffs, NJ, USA: Prentice Hall, 1996, ch. 9, sec. 2, pp. 211–214.

[22] S. Skogestad, and I. Postlethwaite, "Classical feedback control," in *Multivariable feedback control: analysis and design,* 2nd ed. New York, NY, USA: Wiley, 2007, ch. 2, sec. 4, pp. 34–37.

[23] J. A. Butterworth, L. Y. Pao, and D. Y. Abramovitch, "A comparison of ILC architectures for nanopositioners with applications to AFM raster tracking," in *Proc. of American Control Conference.* California, America, 2011, pp. 2266-2271.